

Specific Action as a Metric to Determine Thermal Degradation of Conductive Fabrics Exposed to High Current Impulses

John J. Pantoja^{1, 2, *}, Jorge A. Cristancho¹, Jorge E. Rodriguez¹, Carlos A. Rivera¹, Francisco Román¹, Felix Vega^{1, 2}, Chaouki Kasmi^{2, 3}, and Fahad AlYafei²

Abstract—In this paper, the thermal degradation of electro-conductive fabrics exposed to high current impulses is studied by using an equivalent resistive circuit and a technique commonly applied to the analysis of exploding wires. A method to estimate the threshold burst current of conductive fabrics is derived based on the so-called specific action, which is defined as the integral of the squared current density over the time applied at critical locations of the fabric such as the contact areas between yarns. The model has been experimentally validated on woven and non-woven fabrics using lightning impulse currents applied to the conductive fabrics coated with Cu-Ni alloy. A general rule for determining the dimensions of conductive fabrics as a function of the input-current specific-energy levels has also been derived.

1. INTRODUCTION

Conductive fabrics have been proposed for different applications since their notable characteristics, such as flexibility, high conductivity, low weight, impermeability, and durability. Possible applications reported in the open literature include electromagnetic shielding [1], sensing [2], electrostatic elimination [3], transmission of electrical signals, heating [4], wearable antennas [5], and energy harvesting and storage [6]. They can be used to cover electronic equipment and walls to provide light weight electromagnetic shielding [7] and also to provide multiple functionalities [8]. Normally, electro-conductive textiles are used for low voltage and low current applications; however, there is increasing interest to evaluate their response to higher level currents, such as in the case of fault or lightning current occurrence.

Experimental results have shown that conductive fabrics maintain a conductive behavior at certain levels of current and that melting and bursts are generated at hot spots, producing scratches perpendicular to the current flow [9, 10]. Similar effect was observed in 1960s by Zernow et al. [11], where scratches perpendicular to the current flow on films, denominated as “striation”, were reported in a research about exploding-wires and exploding-films.

These scratches, produced by the conductive layer evaporation, reveal that thermal dissipation and phase change are produced at hot spots, generating a nonlinear behavior from the electrical point of view. This thermal process is described in detail [12] for the case of exploding wires, where the heat-equation solution for bond conductive wires and a method to estimate the burst action (i.e., the specific action required to completely vaporize the conductor material) is presented.

Although different studies on the electrical behavior of conductive fabrics have been reported [4, 15], few of them are related to their capacity to handle high impulse currents and a theoretical description of

Received 23 May 2020, Accepted 25 August 2020, Scheduled 2 September 2020

* Corresponding author: John Jairo Pantoja Acosta (john.pantoja@tii.ae).

¹ Departamento de Ingeniería Eléctrica y Electrónica, Universidad Nacional de Colombia — Sede Bogotá, Bogotá, Colombia.

² Directed Energy Research Centre, Technology Innovation Institute Abu Dhabi, United Arab Emirates. ³ Faculty of Electrical Engineering, Helmut Schmidt University, Hamburg, Germany.

the involved phenomena has not been addressed in depth. An equivalent resistive network was proposed in [13], to model non-woven fabrics, and in [15], to model plain woven fabrics. However, this model did not include a contact resistance between warp and weft yarns, which must be included for low electrical resistance fabrics. An approach similar to [15] is proposed here, however we do take into account the contact resistance since higher energy dissipation is expected in this case. Therefore, based in the calculation of the specific action produced in these contact areas, we describe a procedure to estimate the effects generated by current impulses in fabrics coated with Cu-Ni alloy. Melting, vaporizing, and bursting specific action thresholds of Cu-Ni alloy are also estimated based in its thermo-electrical properties. As shown in Table 1, the use of the Specific action as a quantifier of the thermal degradation of conductive fabrics in impulse current tests and the inclusion of the contact resistance for modeling woven fabrics has not been addressed in previous works on this topic.

Table 1. Models and assessment variables to analyze thermal degradation of conductive fabrics.

Author, year	Model	Assessment variable/ techniques	Ref.
Cristancho et al., 2018	Conductive fabric is modeled as a film conductor.	Energy, peak current.	[9]
Cristancho et al., 2019		Energy, step voltage, Optical microscopy, Scanning Electron Microscopy, Energy Dispersive Spectrometry.	[10]
Dawson et al., 2017	Nonwoven fabric is modeled as an anisotropic sheet network of randomly organized fibers.		[13]
Sarjeant et al., 2007		Current Density, electric field.	[14]
Zhao et al., 2016	Resistive model of conductive woven fabrics based in multiple single yarns connected in parallel in terms of structure, density and yarn arrangement.		[15]
DiSanto et al., 2011		Energy, microphone transducer.	[16]

The paper is organized as follows. The assessment procedure is discussed in Section 2. The equivalent circuit and the sample of conductive fabrics is introduced and described in Section 3. Then, the method is validated with experimental results. The experimental setup is presented in Section 4. Experimental results and comparison with the estimated effects are presented in Section 5. Finally, conclusions are presented in Section 6.

2. ASSESSMENT PARAMETERS

In this section, different assessment parameters to analyze high-current effects and their relationships are presented. Particularly, the Specific Action is introduced and a procedure to estimate this parameter as a function of the melting and boiling points is described and applied for the Cu-Ni alloy case. Therefore, melting, vaporization, and burst thresholds are determined and effects on the tested fabrics are estimated theoretically.

2.1. Assessment Parameters

Different parameters have been used to determine the thermal degradation produced by high current impulses on materials, elements, devices, and systems. On systems, peak current, specific energy, and charge transfer energy are used [17, 18]. On the other hand, peak current, energy density, and specific action are used to estimate the heating of conductive elements and materials [12, 19].

2.1.1. Energy Density

The energy density per volume produced by a current impulse can be calculated as:

$$w = \int \rho(t) j(t)^2 dt, \quad (1)$$

where ρ is the conductor's resistivity, and j is the current density. For high amplitude impulses, both variables in Eq. (1) are time dependent due to the applied current wave form and the resistivity change given by the heating process and material phase transitions.

2.1.2. Specific Energy

Specific Energy (SE), also called action integral [20], is the energy that the stroke converts into 1 Ohm resistance. It can be calculated as:

$$\frac{W}{R} = \int i(t)^2 dt, \quad (2)$$

where W/R is the specific energy of the impulse current i . This parameter is normally used to assess systems against lightning currents.

2.1.3. Specific Action

Specific Action (SA or g) is defined as the integral of the squared current density, j , [19]:

$$g = \int j(t)^2 dt, \quad (3)$$

or as

$$g = \frac{1}{A^2} \int i(t)^2 dt, \quad (4)$$

where A is the initial cross-section area of the conductor. Units of g typically are $A^2 s/mm^4$. This parameter is used to determine the behavior of exploding wires and exploding films and is used here to assess the conductive fabrics.

From the definitions in Eqs. (1) and (3), specific action can be related with energy density by

$$w = \int \rho dg, \quad (5)$$

where dg is the SA differential.

2.2. Estimation of the SA for Melting and Boiling Point of Cu-Ni Alloy

In this section, a procedure to estimate the specific action values for phase transition of Cu-Ni alloy is presented. As reference, we use the specific action thresholds of 22 natural metals for melting, vaporizing, and bursting reported by Tucker and Toth presented in [19].

When a short excitation is applied, heat flow outward the conductor can be neglected in the heat equation [18] and the relationship between specific action and temperature is given by [19]

$$g = C\delta \int \frac{d\theta}{\rho}, \quad (6)$$

where C is the conductive material specific heat, δ the mass density, and θ the temperature. Notice that variations of C and δ with the temperature are neglected.

Below the boiling point, a linear increase of the resistivity can be assumed with the temperature as in [12]:

$$\rho = \rho_0(1 + \alpha\Delta\theta), \quad (7)$$

where ρ_0 is the initial resistivity, α the temperature coefficient of the resistivity, and $\Delta\theta$ the temperature variation. Replacing Eq. (7) in Eq. (6), and integrating, one obtains an equation to calculate the specific action as

$$g = \frac{C\delta}{\rho_0\alpha} \ln(1 + \alpha\Delta\theta). \quad (8)$$

Specific action values obtained using Eq. (8) produce errors below 6% and 15%, respectively, for melting and boiling points as compared with experimental values for Nickel and Copper reported in [19]. These differences could be reduced considering the variation of the thermal parameters with the temperature and including a higher order approximation of the resistivity dependency with the temperature.

Using Eq. (8), the SA of 50/50 Cu-Ni alloy for melting and boiling points were calculated and listed in Table 2. The energy per unit mass, $e = w/\delta$, which can be calculated using the following expression that is obtained taking the derivative of Eq. (6), rewriting, and using Eq. (5), is also tabulated in Table 2.

$$e = C\Delta\theta \quad (9)$$

Table 2. Thermal properties of Cooper, Nickel and Copper-Nickel alloy.

Symbol	Quantity	Units	Cu ⁽ⁱ⁾	Ni ⁽ⁱ⁾	Cu-Ni Alloy ⁽ⁱⁱ⁾
C	Specific heat	J/(g K)	0.38	0.44	0.42
δ	Mass density	g/cm ³	8.96	8.9	8.9
α	Temperature coefficient	$\Omega/(\Omega\text{K})$	0.0043	0.0064	0.0002
ρ_0	Resistivity at 20°C	$\mu\Omega\text{ cm}$	1.7	7	51
ρ_M	Resistivity at melt beginning	$\mu\Omega\text{ cm}$	9.9	59.2	75.9 ⁽ⁱⁱⁱ⁾
ρ_B	Resistivity at burst	$\mu\Omega\text{ cm}$	620	666	
g_M	SA for melting beginning	$\text{kA}^2\text{s/cm}^4$	804	172	89 ^(iv)
g_V	SA for vapor beginning	$\text{kA}^2\text{s/cm}^4$	1240	302	178 ^(iv)
g_B	SA for burst	$\text{kA}^2\text{s/cm}^4$	1730	560	
θ_M	Melting point	K	1357	1726	1483
θ_B	Boiling point	K	2840	3005	3000
e_M	Energy density for melt beginning	J/g	463	807	554 ^(v)
e_V	Energy density for vapor beginning	J/g	1409	1812	1227 ^(v)
e_B	Energy density for burst	J/g	5909	5492	

(i) Specific action and energy density values are taken from [19].

(ii) Cu-Ni alloy thermal properties are based on the data reported in [21].

(iii) Estimated using a linear dependency with the temperature.

(iv) Estimated using (8).

(v) Calculated using (9).

Figure 1 presents the behavior of SA as a function of the energy per unit mass for Copper, Nickel, and 50/50 Cu-Ni alloy. As shown in Fig. 1, the specific action presents a logarithmic growth as the energy density increases. Notice that Cu-Ni alloy and Nickel show a similar behavior.

Resistivities of Copper, Nickel, and Cu-Ni alloy are presented in Fig. 2. The figure shows that the resistivity quickly increases after the conductor begins to vaporize. Thermal and electrical characteristics of these elements are compared in Table 2. The thermal properties of Cu-Ni alloy are based in [21].

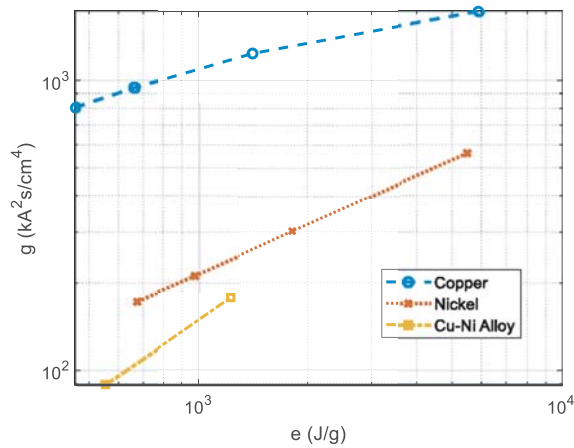


Figure 1. Specific action as a function of the energy per unit mass. Each point, from lower to higher energy, corresponds to the values for melt beginning, melting end, vapor beginning, and burst reported in [19]. Melting and boiling point values for Cu-Ni alloy calculated using (8) and (9) and the temperatures of Table 2 are also included.

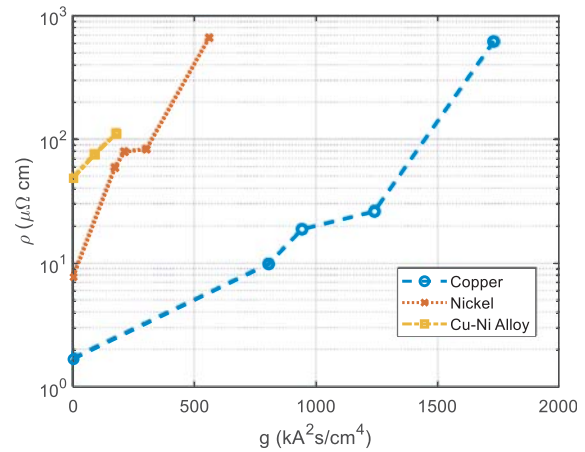


Figure 2. Resistivity as a function of the Specific action. Each point, from lower to higher Specific action, corresponds to the values at melt beginning, melting end, vapor beginning, and burst reported in [19]. Melting and boiling point values for Cu-Ni alloy calculated assuming linear dependency with the temperature are also included.

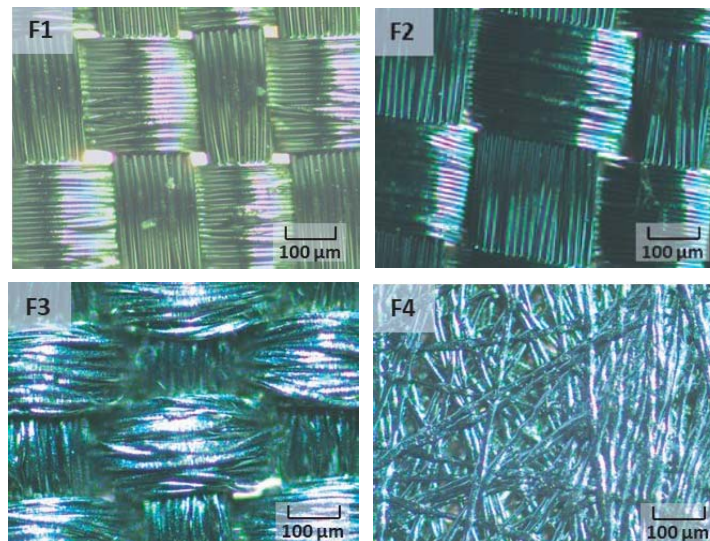


Figure 3. Weave patterns of the tested conductive fabrics: rip-stop (F1), rip-stop with flame retardant (F2), plain (F3), and non-woven weave patterns (F4).

3. ELECTROCONDUCTIVE FABRICS EQUIVALENT CIRCUIT

3.1. Sample of Electroconductive Fabrics

Four types of low-resistivity conductive fabrics were considered. Samples include three woven patterns: rip-stop (here called F1), rip-stop with a layer of flame retardant composite (F2), plain-weave (F3), and one sample of non-woven fabric (F4). See Fig. 3 for reference. Three samples of the same fabric were tested per current level. A total of 12 samples were tested. In all the cases the fabrics were formed on

Table 3. Average dimensions and characteristics of the conductive fabrics' samples.

Symbol	Parameter	Units	F1	F2	F3	F4
ℓ_f	Sample length	cm	10	10	10	10
w_f	Sample width	cm	10	10	10	10
n	Number of fibers in a yarn		48	48	48	-
R	Sample resistance	m Ω /	20	20	33	21
ℓ_s	Woven-section length	μm	250	250	400	-
w_s	Woven-section width	μm	250	250	200	-
s	Conductor thickness	μm	~ 1.5	~ 1.5	~ 1.5	~ 1.5
k	Percentage of width in contact	%	~ 50	~ 50	~ 25	-
s_c	Estimated contact thickness between sections	μm	2	2	3	-
d	Fiber diameter	μm	10	10	10	10
A_s	Conductive cross-section area at the woven section*	mm ²	2.4	2.4	0.88	-
A_c	Conductive cross-section area at yarns contact*	mm ²	0.1	0.1	0.07	-
A_{nw}	Conductive cross-section area for non-woven fabric*	mm ²	-	-	-	1.3
A_{nwp}	Conductive cross-section area for non-woven section with fibers not aligned**	mm ²	-	-	-	0.23

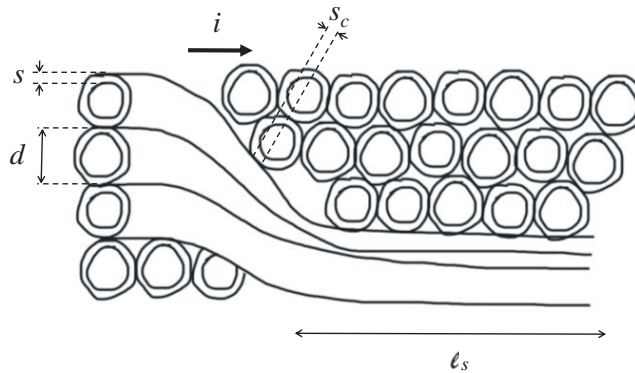
*Cross-section areas are calculated considering a 10 cm wide sample.

**Cross-section area calculated considering a 10 cm wide and 62.5 mm section.

a matrix of polyester fibers coated with Cu-Ni alloy. Physical characteristics of the tested samples are presented in Table 3.

3.2. Equivalent Circuit for Woven Fabrics

Figure 4 shows a cross-section diagram of a woven fabric. Considering the indicated current direction, one can recognize that the transversal area to the flow of current is reduced at the contact areas between the yarns.

**Figure 4.** Cross-section diagram of the contact between two sections on a woven conductive fabric.

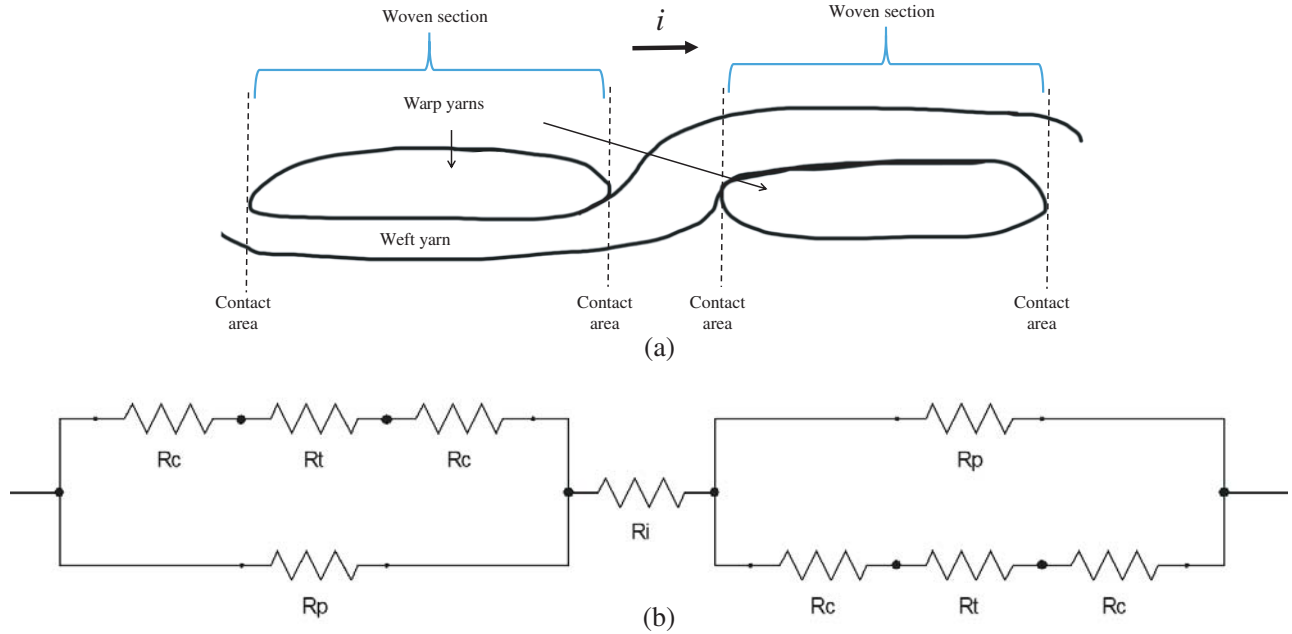


Figure 5. Cut section view of a (a) conductive fabric scheme and (b) its equivalent circuit. Notice that the woven section is decomposed in parallel resistance R_p , contact resistances R_c , and transversal resistance R_t . For squared woven sections, parallel and transversal resistances have similar values.

Figure 5 presents an equivalent circuit for woven fabrics. It can be deduced that the current density is increased in the contact area resistance R_c , which represents the opposition the current flow between warp and weft yarns. In Fig. 5, parasitic inductive and capacitive effects were considered as negligible in the frequency band of interest in this study (fault and lightning induced impulse currents).

As stated in Eq. (4), the SA generated by a current impulse depends on the current waveform and the initial cross-section area of the conductor. The total contact area transversal to the current flow of a woven fabric A_c can be calculated as

$$A_c = w_f k s_c, \tag{10}$$

where w_f is the fabric width, s_c the thickness at the contact area, and k the percentage of the width producing an electrical contact. Considering the cross section geometry of the fibers as circular and the reduction of effective width in the intersection, k is lower than 100%. Notice that this area reduction must be considered to estimate impulse current effects.

On the other hand, the area at a woven section in a fabric A_s can be calculated as

$$A_s = \rho \ell_f / R, \tag{11}$$

where ℓ_f is the fabric length, and R is total fabric resistance.

3.3. Equivalent Circuit for Nonwoven Fabrics

In the case of non-woven fabrics, fibers are randomly oriented. Equation (11) can be used to obtain the average area transversal to the current flow.

Non-woven fabrics can be represented as set of randomly oriented fibers, each one with its own path and its own angle, $\varphi_{f,n}$, from the current propagation axis. Each fiber conductance in the current direction can be calculated as

$$G_{f,n} = G_f \cos \varphi_{f,n}, \tag{12}$$

where G_f is the fiber conductance. Assuming that the length of each fiber is equal to the length of the square material sample, the number of fibers to complete the path is [13]

$$\tilde{n}_n = \frac{1}{\cos \varphi_{f,n}}. \tag{13}$$

Using Eqs. (12) and (13), the conductance of a fiber yields

$$G_{f,n} = \tilde{n}_n G_f \cos^2 \varphi_{f,n}. \quad (14)$$

Including the contributions of the parallel paths of each fiber, the conductance of the square sample can be calculated as [13]

$$G_{fs} \approx \tilde{n}_A G_f \int_{-\frac{\pi}{2}}^{\frac{\pi}{2}} p(\varphi_f) \cos^2 \varphi_f d\varphi_f, \quad (15)$$

where \tilde{n}_A is the total areal density of the square sample, and $p(\varphi_f)$ is the probability distribution function (PDF) of the fibers' angles. Notice that this conductance is the inverse of the total fabric resistance R . Using Eq. (15) and the total fabric resistance, it is possible to calculate partial conductance values for fibers within certain angle range as

$$G_{pnw} \approx \frac{\int_{-\frac{\pi}{2}}^{\varphi_{f,p}} p(\varphi_f) \cos^2 \varphi_f d\varphi_f}{R \int_{-\frac{\pi}{2}}^{\frac{\pi}{2}} p(\varphi_f) \cos^2 \varphi_f d\varphi_f}. \quad (16)$$

Figure 6, for instance, presents the partial conductance calculated using Eq. (16) for a uniform distribution of angles and $R = 0.018$ Ohms. Fig. 6 shows that if fibers with angles below -50° are accumulated in a certain section of the square sample, the partial conductance can be reduced to values lower than 3.75 S, that is resistance higher than 0.26 Ohm. For the case in which these angles are presented in a section of length ℓ_{snw} , the equivalent cross section area normal to the current flow with fibers within this angle range is given by

$$A_{nwp} = \rho \ell_{snw} G_{pnw}. \quad (17)$$

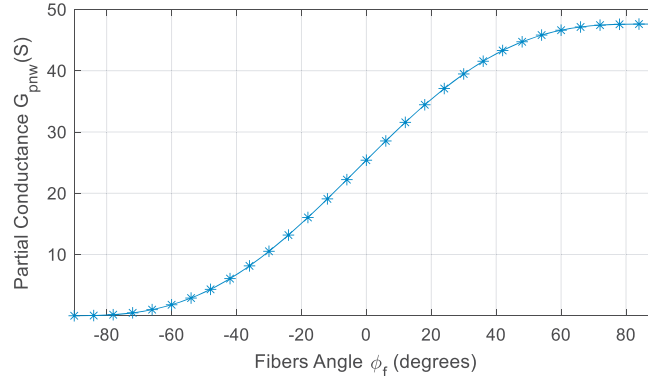


Figure 6. Cumulative partial conductance for a non-woven fabric as a function of the fiber angles calculated using (16) for $R = 0.018$ Ohm and for fiber angles with uniform probability distribution function $p(\varphi_f)$.

4. EXPERIMENTAL SETUP

The conductive fabric samples were tested against current impulses. The effects were registered and are compared with expected effects determined using the SA for each case.

4.1. Circuit Setup

The experimental setup consisted on a lightning impulse current generator (LICG) composed by a $12 \mu\text{F}$ capacitor connected to a spark gap, a $5 \mu\text{H}$ inductance, and the conductive fabric under-test, connected in series as shown in Fig. 7(a).

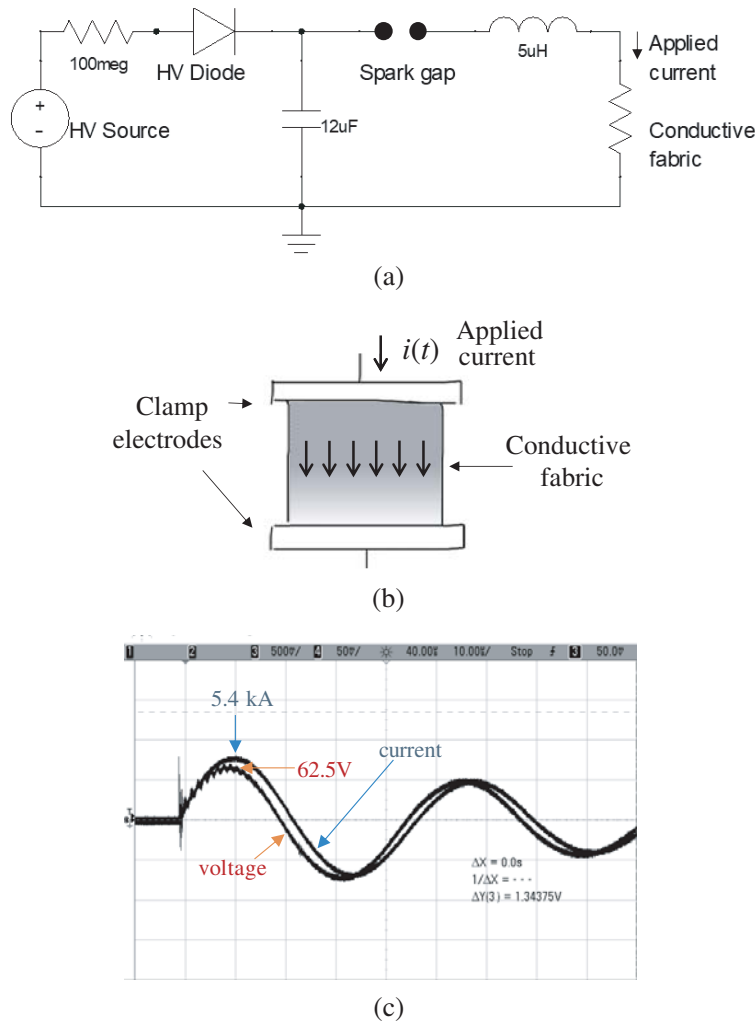


Figure 7. (a) Schematic diagram of impulse current test, (b) details of sample connection during tests, and (c) current and voltage applied to F1 during the first test.

The conductive fabrics were connected with two copper clamp electrodes, as shown in Fig. 7(b). The voltage on the fabric sample was measured using a high voltage probe and the current was measured using a Rogowski coil. Fig. 7(c) shows the current and voltage wave forms obtained for fabric F1 using a charging voltage of 2.1 kV to obtain a peak current of 5.4 kA.

The setup simulates the specific energy of a scaled version of a first positive impulse, with 8 μs rise time and 20 μs half duration time [22]. The circuit was able to produce up to 20 kA peak current; however, here we consider the effects of either 5 kA or 9 kA peak current with, respectively, specific energies around 1 kJ/ Ω and 3 kJ/ Ω . The energy delivered by the circuit with these amplitudes is able to cause change of phase (i.e., melting and vaporization) in the conductive material of fabric samples of 10 cm \times 10 cm [9]. No higher current levels were considered with this sample size since a change of phase indicates the limits of the sample to handle high impulse currents. As stated in Eq. (4), higher current levels can be handled with higher areas. Therefore, for the setup shown in Fig. 7(b), higher current and specific density values will produce similar effects in wider samples.

It is important to mention that in the setup presented in Fig. 7(b), a linear and homogeneous distribution of the current is obtained. In a different scenario; for example, in a single point strike, the energy and current densities decrease radially.

4.2. Expected Effects

According to results on similar experiments, scratches are expected in electroconductive fabrics after testing [9,11]. In order to observe this, photographs of the fabric samples were taken before and after each current impulse. Micrographs and scanning electronic microscope (SEM) images were also taken from selected submillimetric sections of the conductive fabrics after and before high current tests and the results are presented and discussed in [9].

5. RESULTS

Each sample was subject to two consecutive current impulses of 5 kA and 9 kA nominal peak current, in order to differentiate the effects as different SA thresholds are exceeded.

5.1. Observation of Visual Pattern

No visual change was observed on the fabrics after the first current impulse was applied. Therefore, it can be concluded that the current was conducted through the fabrics without generating burns in the surface. Since no visual change was registered for this case in the samples, the photographs are not presented here.

On the other hand, after the second current impulse, superficial scratches perpendicular to the current flow were observed in samples F1, F2, and F3, as shown in Fig. 8. Particularly, F1 presents less scratches than F2 and F3. Notice that not all the contact areas in the samples are burn up, which means that the energy density is different on each contact area. For F4 some dark areas close to bottom electrode were produced, as presented in Fig. 8. The marks close to the electrode can be due to hot spots produced by a deficient electric contact with the electrode. Only one of three tested samples for F4 presented a transversal mark as shown in Fig. 8.

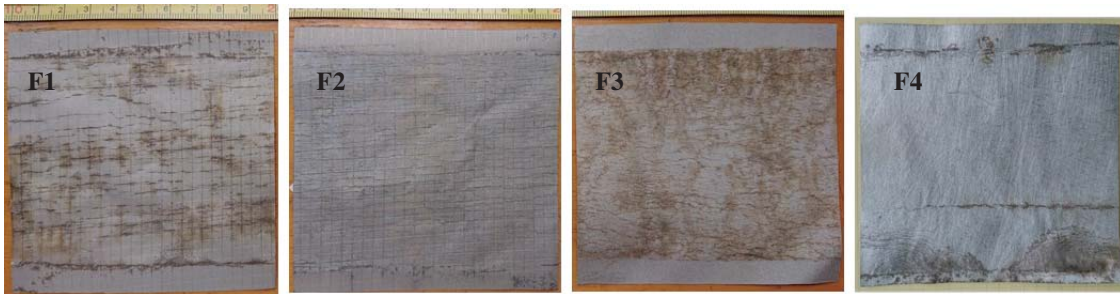


Figure 8. Fabric samples after the impulse current tests. Notice that the electrodes were placed at top and bottom of the samples, where no scratches are presented. Scratches are produced at the electrodes contact and at some point between the electrodes. The current flows from top to bottom.

5.2. Severity Damage Model

We present in this section a comparison between the experimentally-observed and the model-predicted severity damages on the samples.

For the case, the assessment parameters presented in the previous section and the physical characteristics of the conductive fabrics will be used.

The Specific Action will be used as primary assessment parameter, as the resistivity is changing in time and its variation is not uniform in the sample due to hot spot occurrences.

Tables 4 and 5 show the Specific Action calculated for the four types of fabrics at the two peak currents. This was calculated using Eq. (4). The conductive cross-section areas used for calculations were estimated using Eqs. (10) and (11) for woven fabrics and Eqs. (11) and (16) for non-woven fabrics. These cross-section areas and the used parameter values are presented in Table 3. For woven fabrics, SA

Table 4. Estimation of the specific action applied at the first impulse current tests.

Sample	Peak amplitude (kA)	Specific Action ($\text{kA}^2\text{s}/\text{cm}^4$)		
		at woven/average section	at contact area between warp and weft yarns	at area without aligned fibers
F1	5.4	1.7	269.3	-
F2	5.5	1.8	279.4	-
F3	5.1	4.3	427.1	-
F4	5.0	5.4	-	196

Table 5. Estimation of the specific action applied at the second impulse current tests.

Sample	Peak amplitude (kA)	Specific Action ($\text{kA}^2\text{s}/\text{cm}^4$)		
		at woven/average section	at contact area between warp and weft yarns	at area without aligned fibers
F1	8.9	4.9	748.1	-
F2	8.8	4.7	715.2	-
F3	7.9	10.2	1024.8	-
F4	9.5	19.6	-	599

was calculated at the woven sections and at the contact areas between warp and weft yarns; meanwhile, for non-woven fabrics, SA was calculated using the average cross section area and the partial cross section area obtained from Eq. (16) to illustrate the case in which a section of fibers are not aligned with the current direction. A cross-section area of 0.23 mm^2 was calculated using Eq. (16) with uniformly distributed angles below $|\varphi_f| < 50^\circ$ and $\ell_{snw} = 625 \text{ mm}$ to represent the case of the sample shown in Fig. 8.

The SA at contact areas between warp and weft yarns of woven samples was calculated with the help of the equivalent circuit presented in Fig. 5. As shown in that circuit, the current at contact areas has two parallel paths with similar resistances since R_p and R_t have comparable values for squared woven sections. Therefore, assuming that only half the current in a given woven sections flows through the contact resistance R_c and extrapolating this result across the entire sample, the SA for this case can be calculated using half the current amplitude in Eq. (4) and the cross-sectional area of contact between at yarns A_c .

The same results are presented in Fig. 9, alongside the vapor and melting Cu-Ni Specific Action thresholds calculated in Section 3. Therefore, Fig. 9 presents a comparison between the estimated SA in the fabrics for each impulse test and the phase-change thresholds of the conductive layer.

The theoretical results predict that when applying the first impulse, the melting limit (i.e., $89 \text{ kA}^2\text{s}/\text{cm}^4$) is not surpassed at the woven section, for all the four fabrics. However, at the contact area between warp and weft yarns of samples F1, F2 and F3 the $178 \text{ kA}^2\text{s}/\text{cm}^4$ limit is exceeded, meaning that the conductor layer will be reduced, due to evaporation. On the other hand, sample F4 (non-woven fabric) is below the melting limit.

Table 5 and Fig. 9 show the theoretical Specific Action for the second test. Similar to the previous case, the woven section of the four fabrics is below the melting limit. However, at the contact area, the evaporation limit ($178 \text{ kA}^2\text{s}/\text{cm}^4$) is widely surpassed in fabrics F1, F2 and F3. At these values, burst probably occur in the contact areas since the burst limit of Nickel ($560 \text{ kA}^2\text{s}/\text{cm}^4$) is also surpassed. Notice that the non-woven fabric F4 is below the melting threshold for the average section; however,

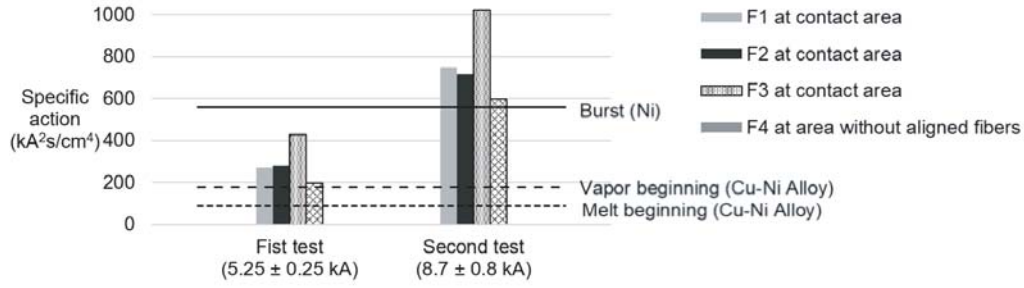


Figure 9. Specific action applied during the impulse tests compared with melting, evaporation, and burst thresholds.

for an area without aligned fibers, the burst limit is exceeded.

These theoretical results are in agreement with the effects observed in the fabrics after the tests. Particularly, F1, F2, and F3 present scratches after the second impulse, which agrees with the calculation of a Specific Action higher than the burst threshold at the contact areas. For illustration in detail, a micrography of a sample of F1 after testing is shown in Fig. 10.

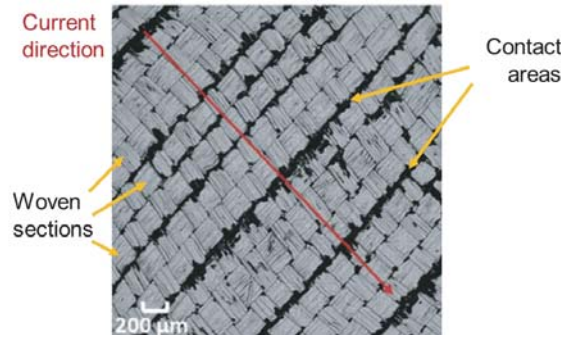


Figure 10. Micrography of a F1 sample after current impulse tests indicating the current direction, unaltered woven sections, and contact areas that have lost the metallic coating.

For F4, it is shown that there is a probability of having some areas in the sample that exceed the burst threshold for the second impulse. This explains the dark line which only appeared in one of the three samples of this type of fabric during the second impulse.

As a conclusion, it can be said that the model was effective for estimating the occurrence of scratches in woven and non-woven electroconductive fabrics. A more detailed representation of the non-woven fabrics is required particularly at the contact area between the planar electrodes used in the tests and the randomly distributed fibers.

5.3. Fabric Width for a Determined Specific Energy Level

For illustration of a practical application of assessment procedure presented here, the cross-section of the tested conductive fabrics required to withstand the flow of a first positive lightning impulse was calculated. Since the thickness is fixed, the width was determined considering that the fabric is used as down conductor and that the current is uniformly flowing across the entire fabric.

Table 6 presents the minimum width of each fabric type for a setup as shown in Fig. 7(b) and the four lightning protection levels (LPL) proposed in [22]. It was calculated by solving Eq. (10) in Eq. (4) for the width w_f and replacing the specific energy of each LPL and the properties of each type of fabric. Table 6 shows that practical widths can be obtained for LPL III and LPL IV if two parallel downstairs based in conductive fabrics are used.

Table 6. Minimum width to avoid burst at contact areas.

Fabric type	LPL I W/R = 10 MJ/ Ω	LPL II W/R = 5.6 MJ/ Ω	LPL III and IV W/R = 2.5 MJ/ Ω	Maximum specific energy per square width (W/R) _{max} /w _f ² (MJ/ Ω /m ²)
F1	8.2 m	6.1 m	4.1 m	0.149
F2	8.2 m	6.1 m	4.1 m	0.149
F3	10.9 m	8.2 m	5.5 m	0.083

A figure of merit of the conductive fabrics can be defined as the maximum specific energy per meter of width squared, as shown in Table 6.

6. CONCLUSIONS

A model based on Specific Action to estimate the effects of current impulses on conductive fabrics was proposed and validated experimentally in this paper. The results of the model anticipated scratches occurrences generated in electroconductive fabrics under high current impulses.

Experimental results and comparisons of applied Specific Action with calculated melting, boiling, and burst thresholds show that woven fabrics concentrate the current at yarns contact areas, generating high energy density and conductor vaporization when the dissipated energy is high enough and the specific action threshold is exceeded.

The results show that non-woven fabrics can better withstand the current impulses, producing less quantity of scratches. However, non-woven fabrics presented showed worst performance at the electrodes position since the electric contact cannot be guarantee with planar electrodes due to the random distribution of the fibers.

Work is in progress to determine the maximum current that could be diverted to the ground by conductive textiles during plasma current phase. In this case, the dimensions of the conducting textiles could be highly reduced.

ACKNOWLEDGMENT

Authors would like to thank Dr. Nicolas Mora from the Directed Energy Research Centre at Technology Innovation Institute for his feedback on this work. This work is partially supported by COLCIENCIAS Convocatoria No. 647/2014 and by Universidad Nacional de Colombia Project No. 37658/2017.

REFERENCES

1. Liu, Z., Y. Yang, X. C. Wang, and Z. Zhou, "Prediction model of shielding effectiveness of electromagnetic shielding fabric with rectangular hole," *Progress In Electromagnetics Research C*, Vol. 48, 151–157, 2014.
2. Terada, T., M. Toyoura, T. Sato, and X. Mao, "Functional fabric pattern — Examining the case of pressure detection and localization," *IEEE Trans. Ind. Electron.*, Vol. 66, No. 10, 8224–8234, Oct. 2019, doi: 10.1109/TIE.2018.2885692.
3. Yamaguma, M. and T. Kodama, "Observation of propagating brush discharge on insulating film with grounded antistatic materials," *IEEE Trans. Ind. Appl.*, Vol. 40, No. 2, 451–456, Mar. 2004, doi: 10.1109/TIA.2004.824512.
4. Tokarska, M., "Characterization of electro-conductive textile materials by its biaxial anisotropy coefficient and resistivity," *J. Mater. Sci. Mater. Electron.*, Vol. 30, No. 4, 4093–4103, 2019, doi: 10.1007/s10854-019-00699-1.

5. Ahmed, M. I., M. F. Ahmed, and A. H. A. M. Shaalan, "Novel electro-textile patch antenna on jeans substrate for wearable applications," *Progress In Electromagnetics Research C*, Vol. 83, 255–265, 2018.
6. Kaushik, V., et al., "Textile-based electronic components for energy applications: Principles, problems, and perspective," *Nanomater. (Basel, Switzerland)*, Vol. 5, No. 3, 1493–1531, Sep. 2015, doi: 10.3390/nano5031493.
7. Rybicki, T., "EMI shielding and reflection from textile mesh grids compared with analytic models," *IEEE Trans. Electromagn. Compat.*, Vol. 61, No. 2, 372–380, Apr. 2019, doi: 10.1109/TEMC.2018.2830968.
8. Kim, H., S. Lee, and H. Kim, "Electrical heating performance of electro-conductive para-aramid knit manufactured by dip-coating in a graphene/waterborne polyurethane composite," *Sci. Rep.*, Vol. 9, No. 1, 1511, 2019, doi: 10.1038/s41598-018-37455-0.
9. Cristancho, J. A., J. E. Rodriguez M., C. A. Rivera G., F. Roman, and J. J. Pantoja, "High current tests over conductive fabrics," *2018 International Conference on Electromagnetics in Advanced Applications (ICEAA)*, 428–432, 2018, doi: 10.1109/ICEAA.2018.8520351.
10. Cristancho, J. A., J. E. Rodriguez, C. A. Rivera, F. Román, L. K. Herrera, and J. J. Pantoja, "Conductive fabric potential rise due to lightning impulse currents," *2019 International Symposium on Lightning Protection (XV SIPDA)*, 1–6, 2019, doi: 10.1109/SIPDA47030.2019.8951605.
11. Zernow, L., F. Wright, and G. Woffinden, "High-speed cinemicrographic studies of electrically exploded metal films," *Exploding Wires*, 245–262, 1962.
12. Chen, K. C.-Y., L. K. Warne, Y. T. Lin, R. L. Kinzel, J. D. Huff, M. B. McLean, M. W. Jenkins, and B. M. Rutherford, "Conductor fusing and gapping for bond wires," *Progress In Electromagnetics Research M*, Vol. 31, 199–214, 2013.
13. Dawson, J. F., A. N. Austin, I. D. Flintoft, and A. C. Marvin, "Shielding effectiveness and sheet conductance of nonwoven carbon-fiber sheets," *IEEE Trans. Electromagn. Compat.*, Vol. 59, No. 1, 84–92, 2017, doi: 10.1109/TEMC.2016.2601658.
14. Sarjeant W. J., et al., "Threshold arcing characteristics for pulsed exploding films," *2007 16th IEEE International Pulsed Power Conference*, Vol. 1, 29–32, 2007, doi: 10.1109/PPPS.2007.4651783.
15. Zhao, Y., J. Tong, C. Yang, Y. Chan, and L. Li, "A simulation model of electrical resistance applied in designing conductive woven fabrics," *Text. Res. J.*, Vol. 86, No. 16, 1688–1700, 2016, doi: 10.1177/0040517515590408.
16. DiSanto, T. M., et al., "Temporal analysis of exploding film burst phenomenon," *IEEE Trans. Plasma Sci.*, Vol. 39, No. 1, 603–607, 2011, doi: 10.1109/TPS.2010.2087776.
17. Smorgonskiy, A., F. Rachidi, M. Rubinstein, N. V Korovkin, and A. P. Vassilopoulos, "Are standardized lightning current waveforms suitable for aircraft and wind turbine blades made of composite materials?," *IEEE Trans. Electromagn. Compat.*, Vol. 59, No. 4, 1320–1328, Aug. 2017, doi: 10.1109/TEMC.2017.2682324.
18. Pantoja, J. J., N. Péna, N. Mora, F. Rachidi, F. Vega, and F. Román, "On the electromagnetic susceptibility of hot wire-based electroexplosive devices to RF sources," *IEEE Trans. Electromagn. Compat.*, Vol. 55, No. 4, 2013, doi: 10.1109/TEMC.2012.2222891.
19. Tucker, T. J. and R. P. Toth, "WBW1: A computer code for the prediction of the behavior of electrical circuits containing exploding wire elements," 1975, doi: 10.2172/4229184.
20. Uman, M. A., *The Art and Science of Lightning Protection*, Cambridge University Press, Cambridge, 2008.
21. "MONEL ® alloy R-405," *Special Metals*, <https://www.specialmetals.com/assets/smc/documents/alloys/monel/monel-alloy-r-405.pdf> (accessed Feb. 13, 2020).
22. "IEC 62305-1 — Protection against lightning — Part 1: General principles," IEC — International Electrotechnical Commission, 2010.